ACS SyntheticBiology

pubs.acs.org/synthbio

Research Article

# Efficient Simulation of Viral Transduction and Propagation for Biomanufacturing

Francesco Destro and Richard D. Braatz*

Cite This: *ACS Synth. Biol.* 2024, 13, 3173−3187

Read Online

ACCESS | Metrics & More | Article Recommendations | Supporting Information

Downloaded via MASSACHUSETTS INST OF TECHNOLOGY on January 11, 2025 at 08:12:04 (UTC).
See https://pubs.acs.org/sharingguidelines for options on how to legitimately share published articles.

**ABSTRACT:** The design of biomanufacturing platforms based on viral transduction and/or propagation poses significant challenges at the intersection between synthetic biology and process engineering. This paper introduces vitraPro, a software toolkit composed of a multiscale model and an efficient numeric technique that can be leveraged for determining genetic and process designs that optimize transduction-based biomanufacturing platforms and viral amplification processes. Viral infection and propagation for up to two viruses simultaneously can be simulated through the model, considering viruses in either the lytic or lysogenic stage, during batch, perfusion, or continuous operation. The model estimates the distribution of the viral genome(s) copy number in the cell population, which is an indicator of transduction efficiency and viral genome stability. The infection age distribution of the infected cells is also calculated, indicating how many cells are in an infection stage compatible with recombinant product expression or viral amplification. The model can also consider the presence of defective interfering particles in the system, which can severely compromise the productivity of biomanufacturing processes. Model benchmarking and validation are demonstrated for case studies of the baculovirus expression vector system and influenza A propagation in suspension cultures.

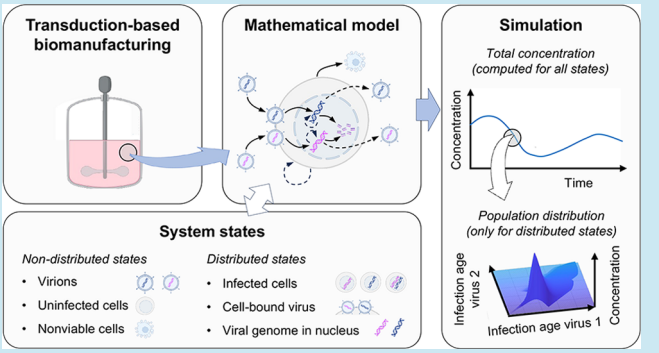


**KEYWORDS:** *biomanufacturing, viral transduction, simulation, continuous manufacturing, baculovirus expression vector system, influenza A*

## 1. INTRODUCTION

Viral transduction through recombinant virus infection is a primary route for gene transfer to producer cells in biomanufacturing. Several types of viruses are used in academic research and industrial practice within transduction-based biomanufacturing platforms.[1] Retroviruses, the most notable example of which are lentiviruses, have been used for producing, among others, virus-like particle (VLP) vaccines[2] and membrane proteins[3] in mammalian cells. Transduction-based expression systems based on baculovirus,[4] adenovirus,[5] or herpes simplex virus[6] have been developed for manufacturing complex products, such as recombinant adeno-associated virus, a primary vector for in vivo gene therapy.[7] Biomanufacturing processes that use phages as transduction vectors have also been explored.[8] Viruses used in transduction-based biomanufacturing can either propagate in the cell culture (e.g., baculovirus) or be replication-deficient (e.g., lentiviral vectors). In other biomanufacturing processes, the viral propagation machinery is solely exploited to amplify viruses of interest to high titers rather than to transfer recombinant genes to the host. For instance, the production of inactivated or live-attenuated virus vaccines for many diseases, including smallpox, polio, measles, and mumps, is based on viral infection and propagation.[9] Furthermore, scalable manufacturing processes for oncolytics and bacteriophages exploit master cell banks and seed virus stocks to produce high titers of the virus through viral amplification.[10,11] In this article, we refer to infection-based biomanufacturing indiscriminately for processes involving only viral transduction, both viral transduction and propagation, or only propagation.

Developing infection-based biomanufacturing systems suitable to large-scale production poses genetic and process engineering challenges due to the complex dynamics of viral infection, virus−host interaction, and recombinant product expression. Synthetic biology tools allow us to engineer the viral and/or host genomes to increase the yield of infection-based manufacturing platforms.[1,12−14] In literature studies, the production of recombinant viruses in mammalian hosts was increased by downregulation of proapoptotic genes[15,16] or by

**Received:** March 30, 2024
**Revised:** August 1, 2024
**Accepted:** September 13, 2024
**Published:** September 24, 2024


© 2024 American Chemical Society

https://doi.org/10.1021/acssynbio.4c00227
*ACS Synth. Biol.* 2024, 13, 3173−3187

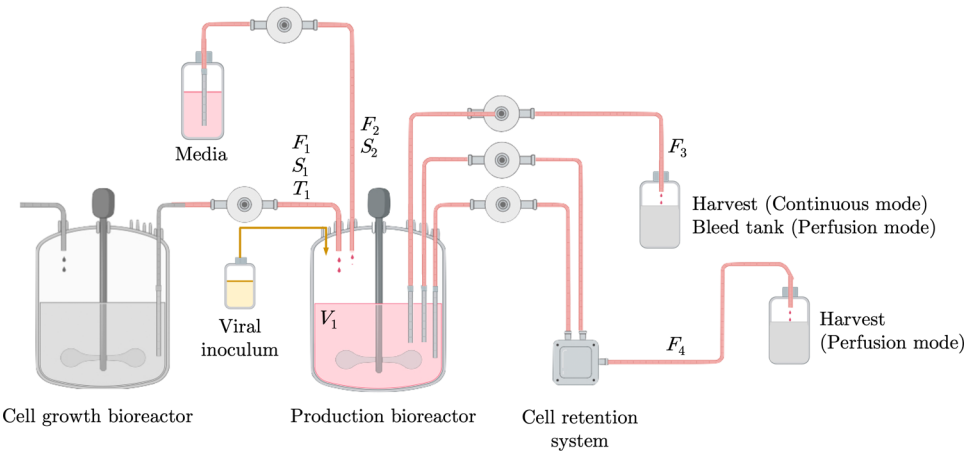


**Figure 1.** Overview of the biomanufacturing process. The model simulates a production bioreactor in batch, perfusion, or continuous mode; shake-flask experiments can also be simulated. The cell growth bioreactor and the harvest and bleed tanks are not simulated but are reported here to clarify the input/output structure of the model when run in continuous or perfusion mode.

overexpression of a vesicle-trafficking protein that increased the cell secretory capacity.[17] Recombinant product yield in the baculovirus expression vector system (BEVS) was boosted through genetic engineering of baculovirus vectors, exploiting transcription and translation enhancers and rational design of the expression cassettes.[14,18,19] The optimization of an infection-based manufacturing system from a process engineering perspective is also a crucial task to achieve high productivity. The optimal multiplicity of infection (MOI) and time of infection (TOI) in batch production depend on a trade-off between preserving a high viable cell density and supplying a high level of genetic template for the product of interest. For manufacturing complex products such as VLPs and viral vectors, cotransduction of multiple viruses carrying different recombinant genes is often necessary. This scenario presents additional challenges since a larger design space has to be optimized. Further complications arise from the formation of defective interfering particles (DIPs),[20] especially for continuous or perfusion processing. DIPs are viruses that lack genetic information essential for self-replication or for recombinant product manufacturing. In cells coinfected by standard virus (STV) and DIPs, the latter can quickly replicate, interfering with STV propagation. DIPs constitute a serious challenge in biomanufacturing since they can become predominant over STVs and halt the production of the desired product.

Mathematical simulation is a powerful tool for enhancing the process[21] and genetic[22−24] design of biomanufacturing platforms. So far, applications of mathematical modeling to enhance infection-based biomanufacturing systems have mainly focused on influenza A.[24−26] Frensing et al.[27] developed a model for influenza A propagation in continuous bioreactors using ordinary differential equations (ODEs) and successfully predicted the insurgence of viral titer oscillations due to STV/DIP competition (Von Magnus effect[28]). Duvigneau et al.[24] developed a mathematical model to guide the genetic engineering of A549 cells for increasing the yield of influenza A propagation. The model describes the main extracellular and intracellular steps of influenza A amplification in a cell culture through differential equations. Duvigneau et al. linked the effect of overexpression of genes CEACAM6, FANCG, NXF1, PLD2, and XAB2 in A549 to the macroscopic kinetic parameters of their model. Training and validation data sets were collected through experiments involving lentiviral transduction of A549 cells to overexpress the relevant genes. The model correctly predicted the effect of overexpression of different gene combinations on product yield in the validation data set. Recently, Rüdiger et al.[29] demonstrated that a model based on partial differential equations (PDEs) tracking the infection age of infected cells can reproduce experimental data from STV/DIP influenza A systems better than lumped parameter models, such as those developed by Frensing and coauthors and Duvigneau and coauthors.

Overall, there is a substantial need for a general framework for simulating infection-based biomanufacturing systems to support the process and genetic design of novel platforms. The underlying mathematical model framework needs to effectively resolve the coupling between extracellular and intracellular events and to be able to account for the presence and competition among different types of viruses. Since the kinetics of viral infection (e.g., binding, replication, and budding kinetics) and recombinant product expression strongly vary with the infection age, models to be leveraged for process design and platform engineering should account for the infection age distribution of the cell population through a system of PDEs.[20,24,30] Fast and accurate numeric schemes are needed for this class of PDE models. This paper presents vitraPro, a computational framework for simulation of viral transduction and propagation that addresses these needs. A multiscale mechanistic model and a novel numerical technique are introduced to simulate viral transduction and propagation in batch, continuous, and perfusion biomanufacturing in the presence of up to two viruses (standard or defective). The framework can simulate any virus/host combination. Two case studies on the BEVS illustrate the use of the computational framework for simulating biomanufacturing platforms based on viral transduction with, respectively, one and two recombinant viruses. The BEVS is chosen as a representative viral system since the baculovirus infection and propagation kinetics are well understood from the literature.[31] A third case study validates the framework with data from the literature on influenza A propagation in the presence of DIPs. The following sections of the paper detail how the computational framework can support the design and optimization of an infection-based biomanufacturing platform from both synthetic biology and process engineering perspectives.


https://doi.org/10.1021/acssynbio.4c00227
ACS Synth. Biol. 2024, 13, 3173−3187

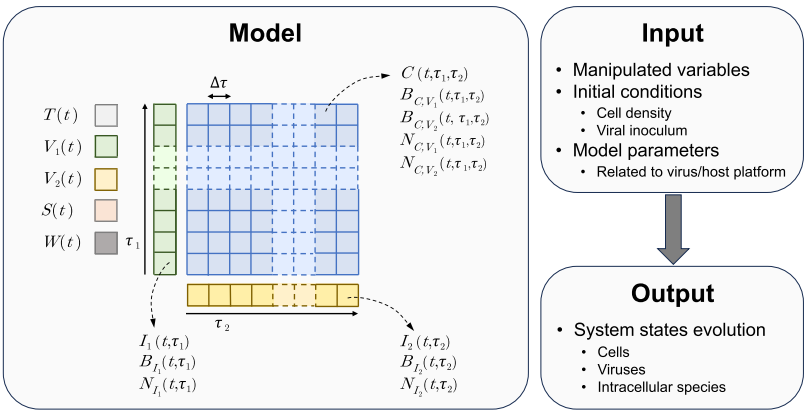


**Figure 2.** Overview of the model structure. Given as inputs the manipulated variable profiles, the initial value of the system states (Table 1), and the model parameters (Table S2), the time evolution of the states is produced as output. The model features 5 ODEs, here represented as standalone squares, and 11 PDEs. Based on the mesh size $\Delta\tau$, the PDEs are converted into sets of ODEs, here represented as sets of contiguous squares. The concentration of cells infected by only one virus ($I_1$ and $I_2$) and the respective amount of surface-bound virus ($B_{I_1}$ and $B_{I_2}$) and nuclear viral genome ($N_{I_1}$ and $N_{I_2}$) are distributed with respect to one infection age (respectively, $\tau_1$ and $\tau_2$). The concentration of coinfected cells ($C$) and the respective amount of surface-bound virus ($B_{C,V_1}$ and $B_{C,V_2}$) and nuclear viral genome ($N_{C,V_1}$ and $N_{C,V_2}$) are distributed with respect to both $\tau_1$ and $\tau_2$.

## 2. RESULTS AND DISCUSSION

**2.1. A Framework for Simulating Viral Transduction and Propagation in Biomanufacturing.** This section summarizes the main features of vitraPro, a novel computational framework for simulating viral transduction or propagation to support the development of biomanufacturing platforms (Figures 1−3). More detailed information is reported in Section 3 and in the Supplementary Methods in the Supporting Information. The computational framework is made up of a mechanistic model and an efficient numerical scheme for solving the model equations. The model simulates viral transduction and/or propagation in batch, perfusion, and continuous cell cultures (in bioreactors or shake flasks; Figure 1) with up to two viral species, including systems with two STVs or one STV and one DIP. Given as input a design for an infection-based biomanufacturing platform, the model estimates through in silico simulations critical variables and key performance indicators (Figure 2 and Table 1). For each virus in the system, the model computes the distributions of infection age and viral genome copy number in the cell culture (Figure 2). The distribution of viral genome(s) copy number predicted by the model directly maps to the copy number of template genome(s) for the product of interest. At the same time, the infection age distribution allows us to infer how many cells are actively expressing genes of interest and, possibly, producing progeny, considering that recombinant product expression and progeny budding occur only during certain phases of viral infection.[6,32] Hence, the combined information from the distribution of infection age and the distribution of viral genome copy number allows us to estimate the concentration of cells in the system that are producing the recombinant product and/or progeny virus and the gene copy number available in each cell for product expression. Furthermore, the model can aid in understanding and forecasting how vector and host designs and process conditions correlate to DIP generation and propagation.

The phenomena considered by the model equations (Figure 3) are viral binding to host cells, viral genome trafficking to the nucleus, degradation, viral replication, progeny production, DIP generation, and viral coinfection dynamics. The model offers a reconciliation between the intracellular and extracellular compartments, which are solved simultaneously with a fast (Table S1) numeric approach that minimizes the detrimental effect of numeric diffusion (see Section 3.2). The distributions of infection age and viral genome copy number computed by the model are leveraged for computing the kinetics of the steps of viral infection that are affected by the infection age and the viral genome copy number, such as viral binding, progeny release, and host viability decay (Figure 4). In the presence of multiple viruses within a cell, the respective infection ages and genome copy numbers are used

**Table 1. Model: Manipulated Variables and System States**[a]

| symbol | UOM | description |
|---|---|---|
| manipulated variables | | |
| $D$ | $h^{-1}$ | dilution rate: batch: $D = 0$; perfusion/continuous: $D > 0$ |
| $r$ | [−] | bleeding ratio: perfusion: $0 \le r < 1$; continuous: $r = 1$ |
| $S_{in}$ | nmol $mL^{-1}$ | substrate concentration in the feed |
| $T_{in}$ | cell $mL^{-1}$ | uninfected cell concentration in the feed |
| system states | | |
| $B_{I_j}(t, \tau_j)$ | virus $mL^{-1}$ | virus $j$ attached to $I_j(t, \tau_j)$, for $j = \{1, 2\}$ |
| $B_{C,V_j}(t, \tau_1, \tau_2)$ | virus $mL^{-1}$ | virus $j$ attached to $C(t, \tau_1, \tau_2)$, for $j = \{1, 2\}$ |
| $C(t, \tau_1, \tau_2)$ | cell $mL^{-1}$ | coinfected cells |
| $I_j(t, \tau_j)$ | cell $mL^{-1}$ | cells infected by virus $j$, for $j = \{1, 2\}$ |
| $N_{I_j}(t, \tau_j)$ | vg $mL^{-1}$ | viral genome $j$ in the nucleus of $I_j(t, \tau_j)$, for $j = \{1, 2\}$ |
| $N_{C,V_j}(t, \tau_1, \tau_2)$ | vg $mL^{-1}$ | viral genome $j$ in the nucleus of $C(t, \tau_1, \tau_2)$, for $j = \{1, 2\}$ |
| $S(t)$ | nmol $mL^{-1}$ | substrate |
| $T(t)$ | cell $mL^{-1}$ | uninfected cells |
| $V_j(t)$ | virus $mL^{-1}$ | extracellular virus $j$, for $j = \{1, 2\}$ |
| $W(t)$ | cell $mL^{-1}$ | nonviable cells |

[a]All system states are expressed as concentrations over the overall system volume. With reference to Figure 1: $D = (F_1 + F_2)/V_1 = (F_3 + F_4)/V_1$, $r = F_3/(F_3 + F_4)$, $S_{in} = (S_1 + S_2)/(F_1 + F_2)$, and $T_{in} = T_1/(F_1 + F_2)$. $\tau_j$ = infection age with respect to virus $j = \{1, 2\}$.


https://doi.org/10.1021/acssynbio.4c00227
ACS Synth. Biol. 2024, 13, 3173−3187

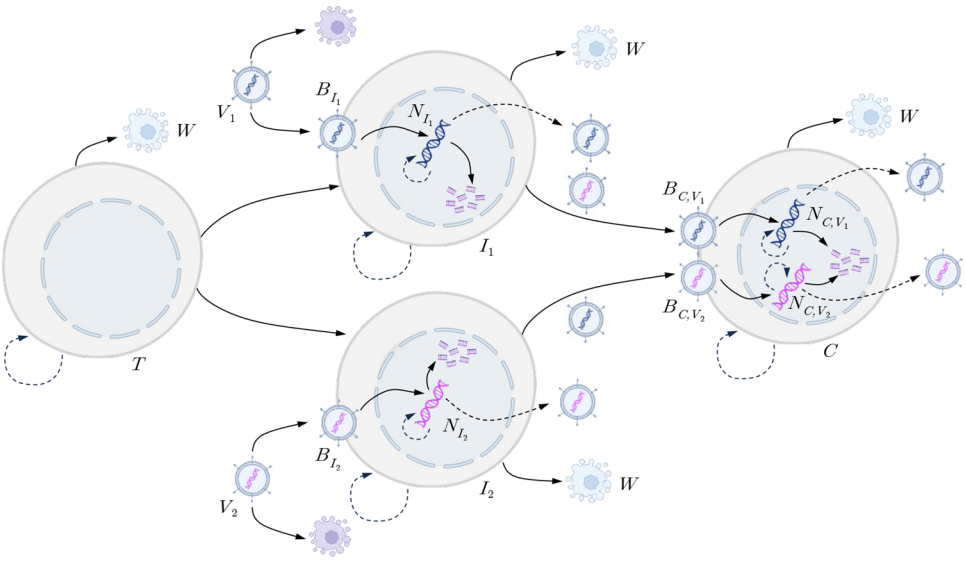


**Figure 3.** Extracellular and intracellular phenomena considered by the model: cell growth, apoptosis and cell lysis, virus binding, virus transport to the nucleus, viral genome replication, viral budding, and degradation of extracellular virus and viral genome. Viral degradation due to rerouting to lysosomes during trafficking to the nucleus is also considered by the model, although it is not reported here for conciseness. The legend of the symbols denoting the system states is reported in Table 1.

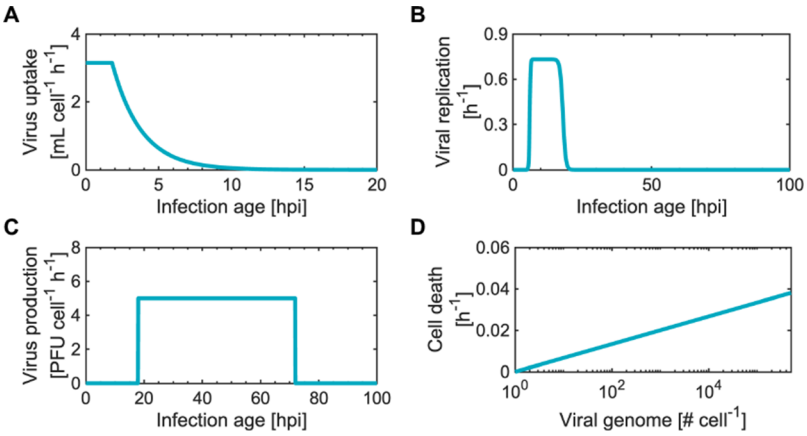


**Figure 4.** Baculovirus infection kinetics: dependency on cell infection age of (A) viral uptake ($\bar{k}_{b,I}V$; eq 3, with viral titer $V$ = 5 PFU per cell), (B) viral replication ($\bar{k}_r$; eq 11), and (C) viral progeny production ($\bar{k}_p$; eq 6). (D) Effect of the viral genome copy number in the cell nucleus on the cell death rate ($\bar{k}_{d,I}$; eq 4). The full list of parameters for the baculovirus infection kinetics is summarized in Table S3.

to simulate the competition between the two viruses for replicating within the host and producing progeny (eqs S14–S24). This architecture allows the simulation of systems with any host/virus combination. Both RNA and DNA viruses with either single-stranded or double-stranded genomes can be considered, as well as viruses infecting hosts through either endocytosis or membrane fusion. Although the model applications are more interesting for systems that involve active viral replication and propagation, the computational framework also can be leveraged for platforms in which no viral replication occurs (e.g., stable integration with lentivirus).

The next sections showcase applications of the computational framework in biomanufacturing systems based on the BEVS and influenza A propagation in the presence of DIPs.

**2.2. Case Study 1: Viral Transduction and Propagation in the BEVS.** This case study focuses on the BEVS to discuss the simulation with vitraPro of infection-based biomanufacturing platforms that exploit only one type of (standard) recombinant virus, assuming that no other standard or defective viruses are present in the system. The BEVS is an established platform for manufacturing high-value products, such as recombinant protein vaccines,[33] VLPs,[34] and viral vectors.[35] In the BEVS, recombinant baculoviruses deliver the genes for a product of interest to producer cells, usually from the Sf9/Sf21 lines derived from *Spodoptera frugiperda*.[36] Figure 5 shows simulations for 10 days of operation in the BEVS with the continuous setup reported in Figure 1. Simulations for three different scenarios are reported, with inoculation at, respectively, MOI = 0.001, 0.1, and 1 plaque-forming unit (PFU) per cell. Case study S1 shows the simulation of batch operation in the BEVS with analogous inoculation conditions (Figure S1 in the Supporting Information). All simulations are obtained using the kinetic parameters for baculovirus infection and propagation estimated in a recent study, which carried out a comprehensive parameter validation with several experimental data sets.[31] For MOI = 1, the infective virus from the inoculum quickly infects a large portion of the cell population and is depleted (Figure 5A–C). Cell infection resumes only


https://doi.org/10.1021/acssynbio.4c00227
ACS Synth. Biol. 2024, 13, 3173–3187

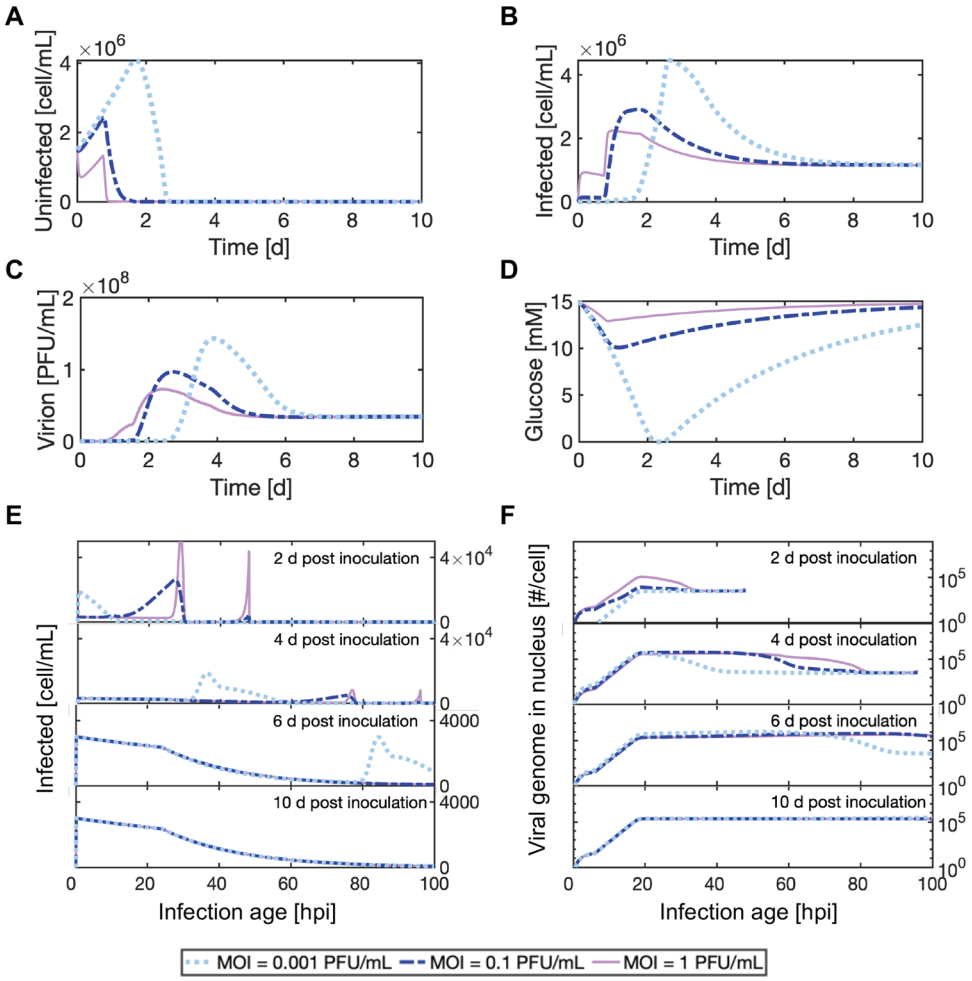


**Figure 5.** Case study 1: viral transduction and propagation in the BEVS. Model simulations for three runs of continuous operation with the BEVS, in a bioreactor inoculated with recombinant baculovirus at, respectively, MOI = 0.001, 0.1, and 1 PFU per cell: (A) uninfected cell concentration, (B) infected cell concentration, (C) virion concentration, (D) glucose concentration, and distributions of (E) infection age and (F) viral genome copy number for the infected cells at 2, 4, 6, and 10 days post-inoculation. Plots (E) and (F) report discrete distributions with a bin size $\Delta\tau = 0.1$ hpi. The additional model outputs from Table 1 are not reported for the sake of conciseness. Complete simulation settings are summarized in Table S6.

when the cells infected by the viral inoculum start producing the progeny virus, approximately 18 h post-infection (hpi). Due to receptor down-regulation induced by baculovirus infection,[36] the rate of viral uptake significantly decreases after infection (Figure 4A). Accordingly, the PFU titer in the system starts increasing only when a small number of uninfected cells are present in the system (Figure 5C). Modest glucose consumption is registered for MOI = 1 (Figure 5D) since baculovirus infection induces cell cycle arrest, reducing (and, eventually, halting) substrate consumption.[36] For MOI = 0.1 and 0.01, only a small fraction of the cell population is infected by the viral inoculum. Uninfected cells continue to grow (Figure 5A) and consume a significant amount of glucose (Figure 5D) for several days until the progeny virus starts budding (Figure 5B). For inoculation at MOI = 0.001, all the glucose in the system is depleted around 2 days after inoculation due to cell growth, despite the continuous glucose feed supplied to the system.

The simulation results also provide insights into the infection age of the cells in the system, breaking down the total concentration of infected cells (Figure 5B) into an infection age distribution (Figure 5E). Two days after viral inoculation, the infection age distribution for MOI = 1 shows a peak corresponding to the cells infected by the inoculum and a shorter peak associated with the cells infected by the viral progeny. Few cells present an infection age intermediate between these two peaks since a low amount of infective virus is present in the system after that the viral inoculum has been uptaken by the cells until the progeny virus starts budding. For MOI = 0.01 and 0.001, the peaks corresponding to the infection wave generated by the viral inoculum are much shorter than those for MOI = 1. The cells infected by the progeny virus, instead, present wider distributions of infection age. Compared to 2 days after inoculation, the infection age distribution moves forward in the infection age axis 4 and 6 days after inoculation, and newly infected cells with low infection age appear in the distribution. The corresponding distribution of viral genome copy number in the nucleus of infected cells (Figure 5F) shows that, at the end of viral replication (≈18 hpi), the infected cells achieve approximately a level of viral DNA within the range of $5 \times 10^4$–$5 \times 10^5$ copies per cell, as found in the literature.[37] About 1 week after inoculation, a steady state is achieved. For all of the considered MOIs at inoculation, the same steady state is reached,


https://doi.org/10.1021/acssynbio.4c00227
ACS Synth. Biol. 2024, 13, 3173−3187

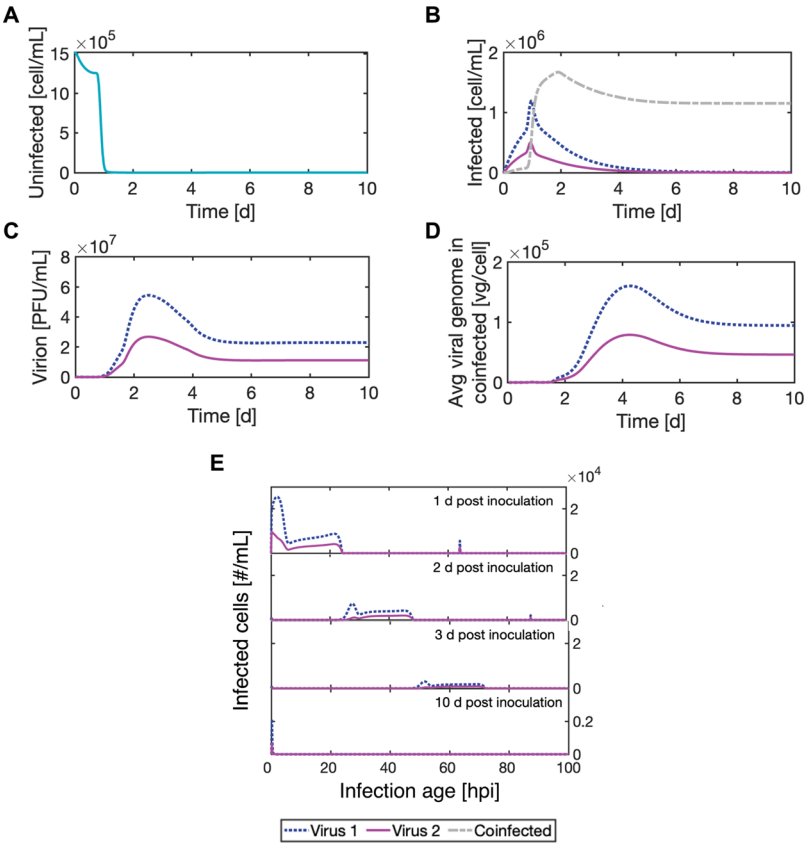


**Figure 6.** Case study 2: viral cotransduction and propagation in the BEVS. Concentrations of (A) uninfected cells, (B) infected cells, (C) virions, and (D) viral genome in coinfected cells (average). (E) Infection age distribution (bin size $\Delta\tau = 0.2$ hpi) of cells infected by only one virus at 2, 4, 6, and 10 days post-inoculation. The complete model output from Table 1 is not reported for the sake of conciseness. Complete simulation settings are summarized in Table S6.

including for the distribution of infection age and of nuclear viral genome for the infected cells.

The benchmarking results of Figures S2−S5 demonstrate that the computational framework presented in this work provides more accurate insights into the dynamics of viral infection and propagation compared to state-of-the-art models for viral systems from the literature. Literature models that do not account for the infection age distribution[27,38] fail to adequately describe continuous and batch experiments in the BEVS since they cannot properly reproduce the viral infection dynamics (Figures S2 and S3). Furthermore, the novel numerical methodology introduced in this work is successful in accurately tracking the baculovirus infection dynamics (Figures S4 and S5). On the contrary, finite difference approaches, traditionally used for computing infection age distributions in viral systems models from the literature,[20,29] fail to accurately track the infection front, due to strong numeric diffusion, for both continuous (Figure S4) and batch (Figure S5) operation.

**2.3. Case Study 2: Viral Cotransduction and Propagation in the BEVS.** The genes necessary for recombinant product manufacturing are oftentimes transferred to producer cells through separate viruses.[6,35,39] The model presented in this work can be used for simulating viral transduction and propagation in the presence of two recombinant viruses to investigate the impact on the productivity of different process designs and of genetic modifications to vectors and hosts. Figures 6 and 7 show a model simulation for a continuous biomanufacturing process based on cotransduction of producer cells by two recombinant viruses (we here refer to cotransduced and coinfected cells interchangeably). Rather than directly using suspended virions, viral inoculation is carried out by introducing infected cells into the bioreactor, as often done in biomanufacturing.[40] The two viruses, denoted as viruses 1 and 2, are two baculoviruses that differ only in the recombinant cassette carried within the same genomic backbone. Cells infected by virus 1 and virus 2 are inoculated at, respectively, 1:100 and 0.5:100 ratios with respect to uninfected cells. The inoculated cells have an infection age of 40 hpi; hence, they start to release the progeny virus soon after inoculation. For the first day after inoculation, the uninfected cells are slowly infected by the progeny of the inoculated infected cells (Figures 6A−D). Most cells infected during the first phase of the process are infected by only either virus 1 or virus 2 (Figure 6B). One day after inoculation, the infection age distribution of the cells infected by only one virus displays a peak at 64 hpi associated with the viral inoculum and a distributed wave of more recently infected cells (Figure 6E). About 1 day after inoculation, the first wave of infected cells starts to produce the progeny virus, which quickly infects the whole cell population. Hence, most cells infected later than 1 day after inoculation are coinfected by both virus 1 and virus 2 (Figures 6B,E and 7A,B). Ten days after inoculation, the coinfected cells (Figure 7C) present the steady-state distribution of infection age expected for baculovirus infection, with a significant decay of viability starting around 24 hpi (Table S4). Interestingly, coinfected cells 10 days after inoculation show a very small difference in infection age


https://doi.org/10.1021/acssynbio.4c00227
ACS Synth. Biol. 2024, 13, 3173−3187

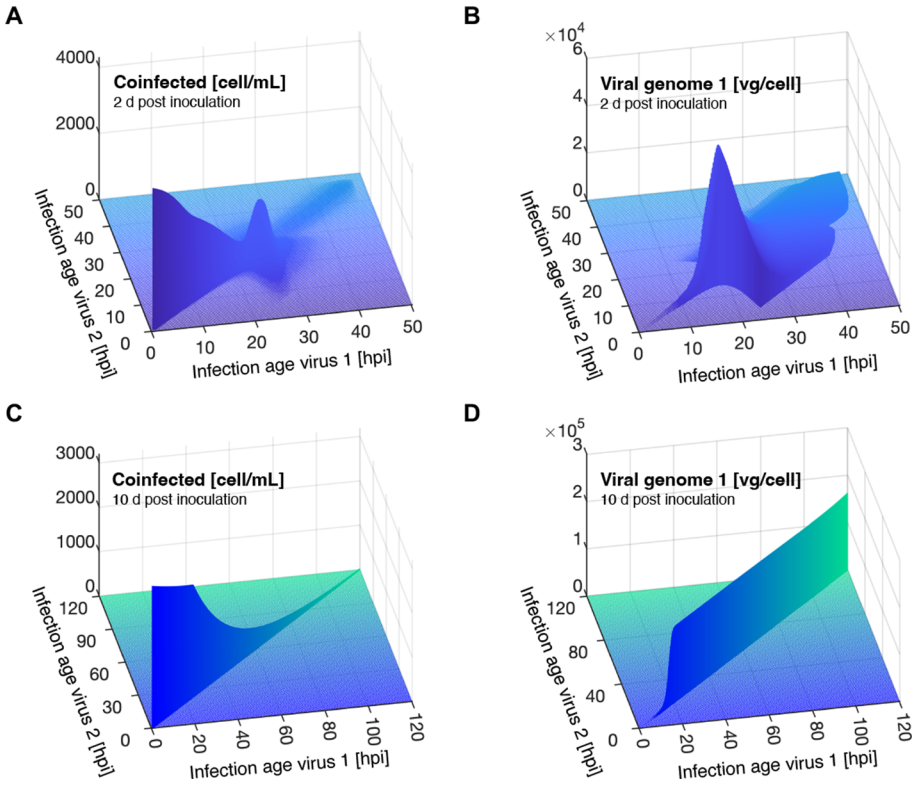


**Figure 7.** Case study 2: sample distributions of infection age and viral genome for coinfected cells. Two days post-inoculation: distributions of (A) infection age and (B) virus 1 copy number. Ten days post-inoculation: distributions of (C) infection age and (D) virus 1 copy number. All figures report discrete distributions with a bin size $\Delta\tau$ = 0.2 hpi. The viral copy number is not reported for bins with a cell concentration lower than 0.1 cell $mL^{-1}$.

between virus 1 and virus 2, indicating that they are coinfected simultaneously, and soon after that, they enter the bioreactor, due to the high viral titer (Figure 6C). The corresponding genome distribution for virus 1 in coinfected cells 10 days after inoculation is reported in Figure 7B. The intracellular viral genome concentration reaches the highest level around 18 hpi, as found in the case study with only one virus (Figure 5E). Cells in infection stages typically associated with recombinant product expression (infection age greater than 15−20 hpi)[32] have approximately 50% more viral DNA copies than the average of the entire population of coinfected cells (Figure 6D).

All simulations discussed in this section and the previous section neglect the formation of DIPs and the loss of recombinant cassettes in the baculovirus genome. These phenomena become significant for the BEVS only for higher passage numbers than those considered so far (15−20 passages in batch operation[41] or approximately 10−15 days after viral inoculation for continuous operation[42]). For longer process durations, DIPs and genome loss can destabilize the steady-state conditions that have been shown for continuous processing in the BEVS; furthermore, DIPs can completely hinder the establishment of a steady state in certain biomanufacturing processes.[27] The next section discusses the simulation of STV/DIP competition through the model presented in this work.

**2.4. Case Study 3: Influenza A Propagation in the Presence of DIPs.** Viral propagation of most DNA and RNA viruses leads to the formation of DIPs, namely virions lacking a large portion of the viral genome and thus incapable of self-replication.[28,43] DIPs can replicate at a faster rate than STVs in STV/DIP coinfected cells, probably due to their shorter genome.[44] As a result, STV/DIP coinfected cells produce a larger DIP than STV progeny, and DIPs can quickly become predominant during serial passage or continuous processing within viral systems. Influenza is one of the viruses for which DIPs have been characterized most extensively.[27,29,45,46] DIPs have been identified as promising candidates for influenza antiviral therapy.[47] However, the formation of DIPs is an adverse event during the production of live attenuated influenza vaccines in immortalized cell cultures since DIPs cause severe titer oscillations that are detrimental to productivity.[27] Rüdiger et al.[29] recently reported experimental data for influenza A propagation in suspension-adapted Madin−Darby canine kidney (MDCK) cells in the presence of DIPs. In batch experiments, MDCK cells were inoculated with different combinations of MOIs of influenza A (H1N1) STVs and DIPs DI244,[48] containing a deletion of the gene coding for the polymerase basic protein 2 (PB2). Twelve experiments were carried out with a full factorial design, using three levels for the STV MOI (0.001, 3, and 30 PFU/mL) and four levels for the DIP MOI (0, 0.001, 3, and 30 PFU/mL). Experimental measurements were collected for viral titers of STVs and DIPs (plaque assay), viable cell density (VCD), fractions of infected and apoptotic cells, and the intracellular viral RNA copy number for STV and DIP, quantified through real-time reverse transcription qPCR (RT-qPCR).

The data reported by Rüdiger et al.[29] are used for validation of the model introduced in this work. Details on modeling and parameter estimation for this case study are reported in Section 3 and in the Supplementary Methods (Supporting Information). The model implementation for the considered influenza


https://doi.org/10.1021/acssynbio.4c00227
ACS Synth. Biol. 2024, 13, 3173−3187

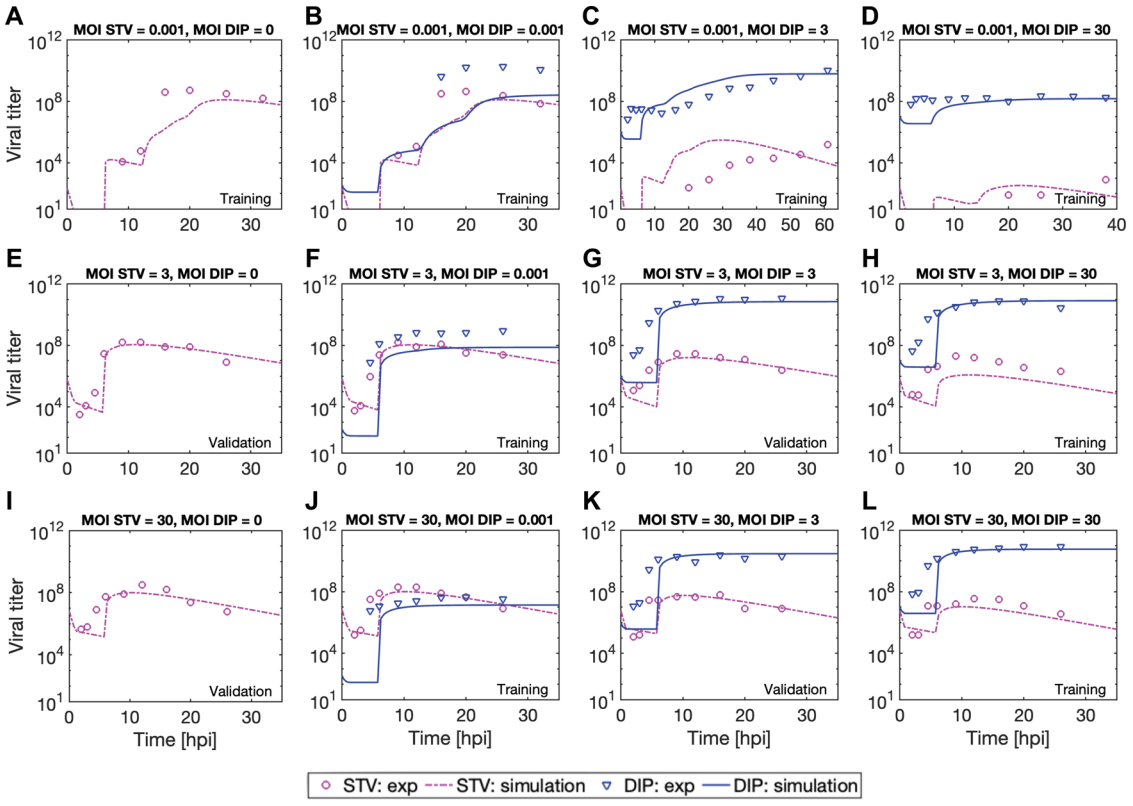


**Figure 8.** Case study 3: influenza A propagation in the presence of DIPs. Model predictions vs experimental measurements for the titers of influenza A STV (infectivity assay) and DIP (real-time quantitative PCR) in 12 batches. Each batch is inoculated at the reported STV MOI, measured through infectivity assays, and DIP MOI, measured through infectivity assays on MDCK cells genetically modified to express PB2 ("active DIP titer" approach[53]). Data from batches (A)−(D), (F), (H), (J), and (L) are used for parameter estimation, while (E), (G), (I), and (K) are used only for model validation. Experimental data are from Rüdiger et al.[29]

A STV/DIP system has 19 equations and 24 adjustable parameters (Table S5). While 13 parameters are directly retrieved from the literature, the remaining 11 parameters are estimated from experimental measurements of infectious STV and total DIP titer (Figure 8), intracellular viral genome copy number (Figure S6), and VCD (Figure S7). Only 8 of the 12 experiments reported by Rüdiger et al.[29] are used for parameter estimation; the remaining 4 experiments are retained as the validation data set. Successful identification of the estimated model parameters is achieved (Table S7). An excellent estimation is achieved for the STV and DIP titers for all of the experiments (Figure 8 and Table S8). The STV and DIP titers are the key variables for this process, since they represent the products of interest for the manufacturing of, respectively, influenza vaccines and DIP antiviral therapy. The model is successful in predicting also the VCD (Figure S7) and the intracellular level of standard and defective viral genome (Figure S6). For the latter, the measurement error can be very significant since the intracellular level of viral genome is inferred through RT-qPCR and VCD signals with a standard deviation of, respectively, 55 and 40%.[49] Measurements of the infected cell concentration are further used for validation (Figure S8). The worst fit for all measurements is achieved in the experiments at an STV MOI equal to 0.001, for which a small measurement error in the inoculated MOI has the largest effect on the experimental dynamics. Furthermore, constant offsets in viral titers and intracellular viral genome measurements, more noticeable at low titers, are expected due to background noise.[29] Hence, the model is successful in predicting the impact of DIPs on STV propagation in all of the experiments, both at the extracellular level and at the intracellular level.

The most advanced model in the state of the art of influenza A STV/DIP systems (and, to the best of our knowledge, of viral transduction and/or propagation systems) has been presented by Rüdiger et al.,[29] in the same article that reports the experiments here considered.[29] The model by Rüdiger et al.[29] contains 132 differential equations and 73 parameters, which summarize and improve a set of models proposed in recent years.[27,49−52] Table S8 compares the residual sum of squared errors (RSS) and the Akaike information criterion (AIC) for the model presented in this work with those for the model by Rüdiger et al.[29] RSS and AIC are calculated on experimental measurements of the key performance indicators for the process: viral titer of (i) STV and (ii) DIP, intracellular viral genome level of (iii) STV and (iv) DIP, and (v) VCD. Rüdiger et al.[29] discussed model validation also for experimental measurements of three mRNA transcripts that intervene during influenza propagation. mRNA measurements are not included in the RSS and AIC computation here, since mRNA and other noncrucial intermediates are lumped together in our model, to reduce the computational burden. The model introduced in this work achieves a better fit than the model by Rüdiger et al.[29] in terms of both RSS and AIC. This result is even more significant considering that the Rüdiger model has 113 differential equations and 49 parameters more than our proposed model. Furthermore, Rüdiger et al. estimated 8 more parameters on the same


https://doi.org/10.1021/acssynbio.4c00227
ACS Synth. Biol. 2024, 13, 3173−3187

experimental data set and used all 12 experiments for parameter estimation. The Supporting Information provides a detailed discussion of the distinctive features of our model that allow this performance. In essence, the computation of the two-dimensional infection age and viral genome copy number distributions (Figure 2), as introduced in this work, allows us to capture the intracellular STV and DIP competition at an unprecedented level of detail, whereas Rüdiger et al. had to heavily rely on heuristic parameters fitted to experimental data to describe the intracellular STV/DIP competition. The novel numerical approach is an enabling feature of the proposed simulation framework, since it allows the propagation of several distributed states in a low computational time and with high accuracy (Table S1). Instead, Rüdiger et al. used a finite difference method that can cause significant errors in the computation of the infection front due to large numerical diffusion.[30]

**2.5. Applications in Genetic Engineering and Process Design.** In infection-based biomanufacturing, viruses are either the product of interest, such as for live attenuated vaccines,[9] oncolytic viruses,[10] and bacteriophages,[11] or they are exploited as transduction agents to express a recombinant product, such as for baculovirus,[4] adenovirus,[5] or herpes[6] vectors. In both cases, the computational framework introduced in this work can be leveraged to enhance the genetic and process design of the biomanufacturing platform.

Genetic engineering of the viral and host genomes can significantly improve the yield of infection-based biomanufacturing processes.[1,12,14−19] The computational framework presented here can indicate bottlenecks in the reaction-transport network of viral infection and propagation that could be enhanced through genetic engineering for improving the process. The model parameters (Table S2) are directly related to factors identified in the literature as critically affecting the process yield, such as specific cell growth rate, viral binding kinetics, latent infection period, and viral budding kinetics.[11] As previously demonstrated for influenza A propagation,[24] certain genetic modifications to a biomanufacturing platform can be correlated to the macroscopic kinetic parameters of the model and used to estimate the effect of a genetic modification on the process yield. This approach can significantly reduce the experimental effort necessary for platform engineering, although it can be adopted only for genetic modifications whose effects on the kinetic parameters of the model are well understood. Since the kinetics of viral infection and progeny production are affected by infection age and viral genome copy number for any virus used in biomanufacturing (Figure 4),[6,13,29,32,38,54] the estimation of infection age and viral genome distributions provided by our model offers useful insights to guide genetic engineering. Notably, the promoters used to express recombinant products are active only during certain infection age intervals in several transduction-based biomanufacturing processes.[32,55] In the BEVS, the commonly used p10 and polh promoters are active, approximately, only 15−20 to 35−50 hpi.[31,32,35,39] The model presented in this work estimates the concentration of cells at infection ages compatible with recombinant product expression (Figures 5E and 7A,C) and the copy number of the recombinant genome in those cells (Figures 5F and 7B,D). Hence, the model can be exploited to maximize the concentration of producer cells and their productivity through synergistic genetic and process optimization. On the contrary, the approximation of infection age and viral genome distribution with the respective averages can be significantly inaccurate (Figures 5E,F, 6D,E, and 7) and bias the estimations of key performance indicators, such as transduced gene copy number, recombinant product expression, and, if relevant, viral progeny production.

From a process engineering perspective, optimization of the operating variables in infection-based biomanufacturing is a challenging task. Due to the high cost necessary for producing the viral inoculum, low-MOI inocula are resorted to in large-scale batch bioreactors. As a result, the whole cell population in the bioreactor becomes infected only through viral propagation, possibly several days after viral inoculation.[40] Meanwhile, uninfected cells grow and consume nutrients present in the system. Specific challenges originate in continuous and perfusion processing, which are innovative approaches for scaling up infection-based biomanufacturing, but require consistently maintaining target viral titers, VCD, nutrient levels, and high product yield during viral propagation.[56,57] The novel simulation framework presented in this work captures this delicate interplay between operating variables, allowing us to predict the dynamics of viral propagation in continuous (Figures 5−7) and batch (Figures 8 and S1) manufacturing better than previously proposed models (Figures S2 and S3 and Table S8), even for inoculation at very low MOIs ($\ll$1). Hence, model simulations can support the optimization of the process conditions in terms of MOI, cell density at the TOI, feed conditions, and media design to increase productivity. For instance, model simulations indicated that the lower productivity per cell, often registered in BEVS-based biomanufacturing at low MOIs,[58] can be influenced by nutrient depletion (Figure S1D), even for continuous processing (Figure 5D). Additionally, model simulations can determine the optimal MOI ratio between multiple viral vectors in cotransduction processes and support the genetic and process design of platforms involving multicistronic vectors or inducible gene expression.

**2.6. Simulation Settings.** A vitraPro simulation is initialized by specifying the initial conditions for the system states, the manipulated variables profiles, the numeric settings, and the model parameters. The simulation settings used for the case studies are reported in Table S6. The model features 16 equations and 64 parameters to describe the most general scenario of cotransduction from two different recombinant viruses (Table S2). The number of parameters reduces to 23 for cotransduction from viruses of the same type that differ only in the recombinant cassette (Table S4, Case study 2) and to 24 to simulate systems with an STV and a DIP of the same type of virus (Table S5, Case study 3). When only one virus is in the system, the model is reduced to 7 equations and 22 parameters (Table S3, Case studies 1 and S1). For viruses and cell lines commonly used in biomanufacturing, most model parameters can be directly retrieved from the literature. As shown in Case study 3, data sets for parameter estimation and model validation can be collected through experiments measuring the VCD, infected cell concentration, infective virion titer, and intracellular viral genome (through PCR or RT-PCR). The model parameters used in the case studies represent reference ranges for most infection-based biomanufacturing platforms (Tables S3−S5). The simulator is expected to be stable for any set of physically relevant values of the model parameters.

On the numeric side, satisfying computational times are achieved in all case studies by using a third-order Runge−


https://doi.org/10.1021/acssynbio.4c00227
ACS Synth. Biol. 2024, 13, 3173−3187

Kutta numeric scheme for integration of the ODEs resulting from PDE discretization (Table S1). A fifth-order Runge−Kutta scheme is also implemented in vitraPro, and it can be used for simulating stiff systems. For nonstiff ODEs, the third-order scheme is recommended for faster computations since it requires fewer function evaluations for a given integration step (the integration step cannot exceed $\Delta\tau$ for the Courant−Friedrichs−Lewy condition, as detailed in Section 3.2). For PDE discretization (Section 3.2), the node size of the infection age mesh ($\Delta\tau$) should be approximately 1 order of magnitude lower than the characteristic time of the fastest infection-age-dependent process. The maximum infection age in the mesh, $\tau_{max}$, should correspond to negligible viability, recombinant product expression, and progeny release. In case these choices of $\Delta\tau$ and $\tau_{max}$ lead to a number of nodes that are computationally intractable, approximated results can be obtained through a coarser mesh. Adjustments might also be needed for the convergence tolerances and scaling settings for simulation conditions very different from those used in the case studies.

**2.7. Model Limitations.** The following limitations should be considered when using the simulation framework. The dynamics of substrate consumption and limitation to growth are implemented for only one (generic) nutrient, which is the nutrient that is present at a limiting level in the system. The model can be extended to consider multiple nutrients and metabolites. Furthermore, a distribution with respect to the infection age might exist for the cell growth rate and specific substrate consumption, which are considered to be constant. However, any model parameter can be converted into functions of infection age and intracellular viral genome level. Although the implementation of such relations in the model would be straightforward, caution must be posed to avoid overfitting and identifiability issues. Case study 3 demonstrates that the current implementation of the model can already explain experimental data with very satisfactory performance. On the contrary, more parameters might be needed to simulate coinfections from two very different viruses that result in strongly nonlinear coinfection kinetics. The intrinsic model limitation to a maximum of two viral species can be tackled by lumping together viruses that present similar kinetics or conducting more simulations, varying the combinations of the multiple viruses that are lumped together into a single viral species. These considerations also apply when more than one type of DIP is present in the system. Unfortunately, the explicit implementation of additional viral species and their infection age as an additional independent variable would make the model too computationally expensive. Finally, the possibility that infected cells can become uninfected due to cell growth and lysosomal degradation is not explicitly considered. Stochastic modeling is needed for properly simulating these phenomena. However, the model considers that these phenomena can reduce the intracellular level of the viral genome, even significantly. In this regard, the viral replication rate should be imposed equal to the cell growth rate for viruses that stably integrate into the host genome.

## 3. METHODS

**3.1. Mathematical Modeling.** The model developed in this work describes viral infection and propagation for up to two viral species in a well-mixed cell culture, operated in batch, continuous, or perfusion mode (Figures 1−3). The model is based on mass balances over the system volume for the species listed in Table 1. The system volume is considered constant in all equations. In this section, all distributed states are introduced as continuous distributions, while the main text reports all distributions in a discrete form. Continuous distributions are represented using lowercase letters for symbols, while discrete distributions are denoted by the corresponding uppercase letters of the same symbol with unchanged subscripts and superscripts. Nondistributed states are always reported as uppercase letters. Section 3.2 details how continuous distributions are converted into discrete distributions. The remainder of this section describes the model for systems presenting only one viral species (used in Case studies 1 and 2). The complete model for systems with two viral species is given in the Supporting Information. The models give completely equivalent results when only one virus is present in the system, although the model for systems with only one virus has a much lower computational demand. The balance for the uninfected cell concentration $T(t)$ [cell/mL] is

$$\frac{dT}{dt} = \mu_T T \frac{S}{K_S + S} - k_{b,T} TV - k_{d,T} T + D(T_{in} - rT) \tag{1}$$

where $\mu_T$ is the growth kinetic constant for uninfected cells, $S$ [nmol/mL] is the substrate concentration in the system, $K_S$ is the Michaelis−Menten constant for substrate limitation to cell growth, $k_{b,T}$ is the kinetic constant for viral binding to uninfected cells, $k_{d,T}$ is the death kinetic constant for uninfected cells, $D$ is the dilution rate of the system, $T_{in}$ is the uninfected cell concentration in the feed, and $r$ is the bleeding ratio. Table 1 clarifies the physical meaning of $D$ and $r$. The terms on the right-hand side of eq 1 account for, from left to right: cell growth, viral infection, cell death, and inlet and outlet from the system. The balance for $i(t, \tau)$ [cell mL$^{-1}$ hpi$^{-1}$], the continuous distribution of the concentration of infected cells with respect to the infection age $\tau$, is

$$\frac{\partial i}{\partial t} + \frac{\partial i}{\partial \tau} = \mu_I i \frac{S}{K_S + S} + k_{b,T} TV\delta(\tau) - i(\overline{k}_{d,I} + rD) \tag{2}$$

where $\mu_I$ is the growth kinetic constant of $i$, $k_{b,T}$ is the binding kinetic constant for uninfected cells, $\overline{k}_{d,I}$ is the death equivalent kinetic constant for infected cells, and $\delta(\cdot)$ is the Dirac delta function, which ensures that the contribution from newly infected cells is considered at the boundary ($\tau = 0$). The terms on the right-hand side of eq 2 account for, from left to right: cell growth, infection of uninfected cells, cell death, and outlet from the system. For most viral species, infected cells undergo cell cycle arrest ($\mu_I = 0$). The binding equivalent kinetic constant for infected cells ($\overline{k}_{b,I}$) depends on $\tau$,

$$\overline{k}_{b,I}(\tau) = \begin{cases} k_{b,T}, & \text{for } \tau < \tau_b \\ k_{b,T}\exp(-\beta_b(\tau - \tau_b)), & \text{for } \tau \geq \tau_b \end{cases} \tag{3}$$

where $\beta_b$ and $\tau_b$ are suitable coefficients that describe the viral binding downregulation with the progress of the infection age, which is experienced for most viral infections.[59,60] The death equivalent kinetic parameter depends on both the infection age and the viral genome copy number:[31]


https://doi.org/10.1021/acssynbio.4c00227
ACS Synth. Biol. 2024, 13, 3173−3187

$$\overline{k}_{d,I}(t,\tau) = \begin{cases} k_{d,T}, & \text{for } \tau < \tau_d \\ k_{d,I}\ln(n/i) & \text{for } \tau \geq \tau_d \end{cases} \quad (4)$$

where $k_{d,I}$ is the death kinetic constant for infected cells, $\tau_d$ is the infection age at which an increase of death rate is registered for infected cells, and $n/i$ is the viral genome copy number in the nucleus of cells, as further discussed. Equation 4 establishes a dependence of the death rate of infected cells $i(t, \tau)$ from the intracellular level of the viral genome. The balance for extracellular virions $V(t)$ is

$$\frac{dV}{dt} = \int_0^\infty \overline{k}_v i d\tau - k_{b,T}TV - \int_0^\infty \overline{k}_{b,I} iV d\tau - k_{d,V}V - DV \quad (5)$$

where $k_{d,V}$ is the degradation kinetic constant for extracellular virions, and $\overline{k}_v$ is the progeny release equivalent parameter. The terms on the right-hand side of eq 5 represent, from left to right: virion production from infected cells, viral infection of uninfected cells, viral infection of already-infected cells, degradation of extracellular virions, and outlet from the system. The progeny release per cell depends on the infection age:

$$\overline{k}_v(\tau) = \begin{cases} 0, & \text{for } \tau < \tau_v^{on} \vee \tau > \tau_v^{off} \\ k_v, & \text{for } \tau_v^{on} \leq \tau \leq \tau_v^{off} \end{cases} \quad (6)$$

where $k_v$ is the progeny release rate, and $\tau_v^{on}$ and $\tau_v^{off}$ define, respectively, the upper and lower bound of the infection age interval during which the viral progeny is released. Equation 6 represents an effective way of lumping together several steps of the intracellular pathway that occur between the infection of a cell and the onset of progeny release. For simplicity, the presence of only one substrate $S$ is considered in the default implementation of the model. The mass balance for $S(t)$ is

$$\frac{dS}{dt} = D(S_{in} - S) - \frac{S}{\phi_S + S}\left(Y_{S,T}T + \int_0^\infty Y_{S,I} i d\tau\right) \quad (7)$$

where $S_{in}$ is the substrate concentration in the feed, $Y_{S,T}$ is the specific substrate consumption for $T$, $Y_{S,I_1}$ is the specific substrate consumption for $i_1$, $Y_{S,I_2}$ is the specific substrate consumption for $i_2$, $Y_{S,C}$ is the specific substrate consumption for $c$, and $\phi_S$ is a parameter describing the kinetics of substrate consumption at low substrate levels, which is fixed to $\phi_S = 0.01$ nmol mL$^{-1}$ in this work. A balance is also developed for tracking the concentration of nonviable cells $W(t)$ in the system:

$$\frac{dW}{dt} = k_{d,T}T + \int_0^\infty \overline{k}_{d,I} i d\tau - W(k_{lys} + rD) \quad (8)$$

where $k_{lys}$ is the lysis kinetic constant for nonviable cells. Species $W$ considers all nonviable cells lumped together independently of whether they were infected or not.

The model calculates the concentration of two intracellular species: $b(t, \tau)$, the virus bound to the surface of infected cells, and $n(t, \tau)$, the viral genome in the nucleus of a cell. Both $b(t, \tau)$ and $n(t, \tau)$ are computed with respect to the whole volume of the system, namely with the unit of measurement [#mL$^{-1}$ hpi$^{-1}$]. This choice allows tracking the number of viruses uptaken by every cell more accurately and also leads to greater numeric robustness. Notably, under the deterministic modeling assumptions followed here, cells infected at the same time instant will inherently present the same $b(t, \tau)$ and $n(t, \tau)$ profiles with the progress of time (until cell death). Hence, distributions $b(t, \tau)$ and $n(t, \tau)$ directly map to the distribution of cells with respect to infection age $i(t, \tau)$. Normalization of $b(t, \tau)$ and $n(t, \tau)$ by $i(t, \tau)$ allows us to convert the concentration of the intracellular species into distributions expressed in a per cell basis [#/cell]. The model assumes irreversible viral attachment; hence, a cell is considered infected as soon as a virus bounds to its surface. Species $b$ can represent viruses either bound to receptors or directly attached to the cell membrane. The model parameters that govern viral binding inherently account for the trade-off between binding and unbinding rates. The balance for $b(t, \tau)$ is

$$\frac{\partial b}{\partial t} + \frac{\partial b}{\partial \tau} = V(k_{b,T}T\delta(\tau) + \overline{k}_{b,I}I) - b(k_i + rD + \overline{k}_{d,I}) \quad (9)$$

where the terms on the right-hand side of the equation represent, from left to right: viral binding to uninfected cells, viral binding to infected cells, internalization of surface-attached viruses through kinetic constant $k_i$, outlet from the system, and death of infected cells. The last term is included to remove from the mass balance the amount of virus bound to the surface of infected cells that die since $b$ represents the cumulative amount in the system of virus bound to (viable) infected cells. The model considers trafficking to the nucleus as a single lumped step. This simplification is introduced to reduce the computational burden of the model, especially for its two-dimensional implementation. This modeling choice does not significantly degrade the model's predictive performance, as long as $k_i$ is taken as the kinetic parameter for the rate-determining step within the pathway of trafficking to the nucleus. The balance for $n(t, \tau)$ is

$$\frac{\partial n}{\partial t} + \frac{\partial n}{\partial \tau} = \eta k_i b - n(\overline{k}_{d,I} + k_{d,N} - \overline{k}_r + rD) \quad (10)$$

where the terms on the right-hand side represent, from left to right: trafficking to the nucleus, contribution due to cell death (as for $b$), degradation of the viral genome in the nucleus (with kinetic parameter $k_{d,N}$), viral replication, and outlet of infected cells from the system. Parameter $\eta$ represents the fraction of internalized virus that reaches the nucleus and also accounts for rerouting to lysosomes. The effective replication kinetic parameter $\overline{k}_r(\tau)$ is calculated as

$$\overline{k}_r(\tau) = \begin{cases} 0, & \text{for } \tau < \tau_r^{on} \vee \tau > \tau_r^{off} \\ k_r, & \text{for } \tau_r^{on} \leq \tau \leq \tau_r^{off} \end{cases} \quad (11)$$

where $k_r$ is the viral genome replication kinetic constant, and $\tau_r^{on}$ and $\tau_r^{off}$ define, respectively, the upper and lower bound of the infection age interval during which viral amplification occurs. Equation 11 represents an efficient way of lumping together several steps of the intracellular pathway for viral amplification. Notably, $\overline{k}_r$ should be set to be equal to the cell growth rate for viruses that integrate into the host genome. The set of eqs 1, 2, 5, and 7−10 represents the model for systems with one viral species. The list of model parameters is summarized in Table S3.

**3.2. Numerics.** A decoupled integration-reallocation numerical scheme is introduced in this work. The model


https://doi.org/10.1021/acssynbio.4c00227
ACS Synth. Biol. 2024, 13, 3173−3187

equations are integrated with the method of lines by discretizing the PDEs into ODEs along the infection age coordinate(s) (Figure 2). During integration, infection ages are assumed not to vary. Separately, a reallocation routine accounts for the increase of infection age, as further discussed. The numerical scheme is first described in detail for the simplified model for systems with one viral species, outlined in the previous section. The infection age $\tau$ is discretized into $L$ nodes. All nodes have a size $\Delta\tau$, except for node $L$, which corresponds to the interval $[\tau_{max}, \infty)$ in the original space of the continuous variable $\tau$. The maximum infection age $\tau_{max}$, arbitrarily selected, is an infection age associated with very low cell viability as well as negligible recombinant product expression and progeny release. Mesh nodes $l$ = 1, 2, 3, ..., and $L$ have infection age $\tau^l$ = 0, $\Delta\tau$, $2\Delta\tau$, ..., and $\tau_{max}$. The distributed states $b(t, \tau)$, $i(t, \tau)$, and $n(t, \tau)$ are discretized with respect to $\tau$ into the sets of $L$ states denoted as, respectively, $B(t, \tau^l) = B^l$, $I(t, \tau^l) = I^l$, and $N(t, \tau^l) = N^l$, for $l$ = 1, 2, ..., $L$. The model PDEs (eqs 2, 9, and 10) are converted into the sets of ODEs:

$$\frac{dI^l}{dt} = \mu_I I^l \frac{S}{K_S + S} + k_{b,T} T V \delta_{l1} - I^l(\overline{k}_{d,I} + rD), \quad \text{for } l = 1, 2, \ldots, L \tag{12}$$

$$\frac{dB^l}{dt} = V(k_{b,T} T \delta_{l1} + \overline{k}_{b,I} I^l) - B^l(k_i + rD + \overline{k}_{d,I}), \quad \text{for } l = 1, 2, \ldots, L \tag{13}$$

$$\frac{dN^l}{dt} = \eta k_i B^l - N^l(\overline{k}_{d,I} + k_{d,N} - \overline{k}_r + rD), \quad \text{for } l = 1, 2, \ldots, L \tag{14}$$

where $\delta_{l1}$ is the Kronecker delta function. Equations 12−14 do not account for the $\frac{\partial I}{\partial \tau}$, $\frac{\partial B}{\partial \tau}$, and $\frac{\partial N}{\partial \tau}$ contributions in eqs 2, 9, and 10 but present otherwise the same contributions of the original PDEs. The integrals in eqs 5,7, and 8 are converted into sums across all mesh nodes. The ODE/PDE system of eqs 1, 2, 5, and 7−10 becomes the system of ODEs of eqs 1, 5, 7,8, and 12−14, which are integrated with a Runge−Kutta scheme with adaptive time stepping. Both third-order and fifth-order Runge−Kutta schemes are available in the simulator. At every integration step $i$, the cumulative sum of the integration steps ($s_i$) is updated with the $i$th integration step $h_i$ as

$$s_i = s_{i-1} + h_i \tag{15}$$

where $s_0$ is initialized to 0. At the end of each integration step $i$, if the condition

$$s_i = \Delta\tau \tag{16}$$

is met, then $I^l$, $B^l$, and $N^l$ (for $l$ = 1, 2, ..., $L$) are reallocated along the mesh to account for the increase of infection age, with the following procedure. Defining the value of the states $I^l$, $B^l$, and $N^l$ in every mesh node at the end of integration step $i$ as, respectively, $I^{l,i,fin}$, $B^{l,i,fin}$, and $N^{l,i,fin}$, the corresponding initial value of the states for integration step $i$ + 1 (respectively, $I^{l,i+1,in}$, $B^{l,i+1,in}$, and $N^{l,i+1,in}$) is calculated as

$$I^{1,i+1,in} = 0,\ B^{1,i+1,in} = 0,\ N^{1,i+1,in} = 0 \tag{17}$$

$$I^{l,i+1,in} = I^{l-1,i,fin},\ B^{l,i+1,in} = B^{l-1,i,fin},\ N^{l,i+1,in} = N^{l-1,i,fin}, \text{ for } l = 2, 3, \ldots, L-1 \tag{18}$$

$$I^{L,i+1,in} = I^{L-1,i,fin} + I^{L,i,fin},\ B^{L,i+1,in} = B^{L-1,i,fin} + B^{L,i,fin},\ N^{L,i+1,in} = N^{L-1,i,fin} + N^{L,i,fin} \tag{19}$$

The integration step counter $i$ is then reinitialized to 0. At the end of every integration step $i$ in which Condition 16 is not met, $I^{l,i+1,in}$, $B^{l,i+1,in}$, and $N^{l,i+1,in}$ correspond, for every mesh node $l$, to, respectively, $I^{l,i,fin}$, $B^{l,i,fin}$, and $N^{l,i,fin}$. The described integration-reallocation steps are iteratively repeated during the simulation. In the simulation routine, the integration step $h_i$ is automatically constrained not to exceed $\Delta\tau$, to respect the Courant−Friedrichs−Lewy condition.

The model for systems with two viruses is solved with an analogous approach. The continuous variables $\tau_1$ and $\tau_2$ are both discretized into $L$ mesh nodes (respectively, $\tau_1^l$ and $\tau_2^l$, for $l$ = 1, 2, ..., $L$). All nodes have a size $\Delta\tau$, except for $\tau_1^L$ and $\tau_2^L$, which correspond to the interval $[\tau_{max}, \infty)$ in the original space of $\tau_1$ and $\tau_2$. The distributed states are discretized with respect to $\tau_1$ and $\tau_2$, as shown in Figure 2. To simplify the notation, the $\tau_1^l$ and $\tau_2^l$ notation is dropped and, instead, it is postulated that $\tau_1$ and $\tau_2$ can only assume discrete values when they refer to discrete distributions (denoted by uppercase letters). Accordingly, the integrals over the infection age(s) in the model equations (eqs S9 and S10) are converted into sums across all mesh nodes. The PDEs corresponding to distributed states (eqs S2, S3, S6, and S15−S22) are converted into sets of ODEs, as outlined for the model for systems with one virus. The ODEs resulting from the discretization are solved together with the other ODEs of the model (eqs S1, S9, and S10), with an integration-reallocation approach. The reallocation for states distributed with respect to only $\tau_1$ or $\tau_2$ (i.e., $I_1$, $I_2$, $B_{I_1}$, $B_{I_2}$, $N_{I_1}$, and $N_{I_2}$) is carried out with a procedure analogous to eqs 17−19. States distributed with respect to both $\tau_1$ and $\tau_2$ (i.e., $C$, $B_{C,V_1}$, $B_{C,V_2}$, $N_{C,V_2}$, and $N_{C,V_2}$) are reallocated along both $\tau_1$ and $\tau_2$ simultaneously, resulting in diagonal movements along the mesh (Figure 2). Boundary conditions analogous to eqs 17 and 19 are imposed also for the states distributed to both infection ages. Finally, the viral binding downregulation experienced for most viral infections (eq 3) is exploited to reduce the computational burden. A parameter $\tau_{b,max} \leq \tau_{max}$ is defined based on the viral binding decay profile with respect to the infection age for the considered viral system. In all equations distributed with respect to one or more infection ages, the contributions from viral binding are not computed in mesh nodes, where the infection age is equal to or greater than $\tau_{b,max}$. Furthermore, the nodes of the 2D infection age mesh in which $|\tau_1 - \tau_2| \geq \tau_{b,max}$ cannot be accessed by any species. The corresponding states are set to 0 for every value of $t$, and the associated ODEs are not computed. This approach for reducing the number of equations of the model is not used if DIPs are present in the system since, typically, DIP-infected cells can always be reinfected, independently from the infection age with respect to DIPs.

**3.3. Simulations.** The results presented here were generated with a MATLAB implementation of the model



https://doi.org/10.1021/acssynbio.4c00227
ACS Synth. Biol. 2024, 13, 3173−3187

and the numerics introduced in this work. The simulation settings are summarized in Table S6 for all case studies. The model for systems with one virus is used in Case studies 1 and S1, while the model for systems with two viruses is used in Case studies 2 and 3. The Supporting Information provides additional information about the simulation settings and parameter estimation strategies used in the case studies.

## ■ ASSOCIATED CONTENT

### Data Availability Statement

MATLAB and Python implementations of the simulator presented in this work can be downloaded at https://github.com/francescodestro/vitraPro. The repository also contains the code used for generating all the results of the case studies.

### Supporting Information

The Supporting Information is available free of charge at https://pubs.acs.org/doi/10.1021/acssynbio.4c00227.

Case study S1, additional model benchmarking, list of model parameters, simulation settings used in the case studies, additional discussion on Case study 3, and supplementary methods (PDF)

## ■ AUTHOR INFORMATION


### Corresponding Author

**Richard D. Braatz** − *Massachusetts Institute of Technology, Cambridge, Massachusetts 02139, United States;* orcid.org/0000-0003-4304-3484; Email: braatz@mit.edu

### Author

**Francesco Destro** − *Massachusetts Institute of Technology, Cambridge, Massachusetts 02139, United States;* orcid.org/0000-0002-0977-0672

Complete contact information is available at: https://pubs.acs.org/10.1021/acssynbio.4c00227


### Author Contributions

F.D.: conceptualization, formal analysis, investigation, methodology, software, validation, visualization, writing—original draft, writing—review and editing. R.D.B.: conceptualization, methodology, writing—original draft, writing—review and editing, supervision, funding acquisition.

### Notes

The authors declare no competing financial interest.

## ■ ACKNOWLEDGMENTS

This work was done in Cambridge, MA, USA. This work was supported by the U.S. Food and Drug Administration through contract no. 75F40121C00131.

## ■ REFERENCES


(1) Rodrigues, A. F.; Carrondo, M. J.; Alves, P. M.; Coroadinha, A. S. Cellular targets for improved manufacturing of virus-based biopharmaceuticals in animal cells. *Trends Biotechnol.* **2014**, *32*, 602−607.

(2) Fontana, D.; Kratje, R.; Etcheverrigaray, M.; Prieto, C. Rabies virus-like particles expressed in HEK293 cells. *Vaccine* **2014**, *32*, 2799−2804.

(3) Elegheert, J.; Behiels, E.; Bishop, B.; Scott, S.; Woolley, R. E.; Griffiths, S. C.; Byrne, E. F.; Chang, V. T.; Stuart, D. I.; Jones, E. Y.; Siebold, C.; Aricescu, A. R. Lentiviral transduction of mammalian cells for fast, scalable and high-level production of soluble and membrane proteins. *Nat. Protoc.* **2018**, *13*, 2991−3017.

(4) Felberbaum, R. S. The baculovirus expression vector system: A commercial manufacturing platform for viral vaccines and gene therapy vectors. *Biotechnology J.* **2015**, *10*, 702−714.

(5) Chadeuf, G.; Favre, D.; Tessier, J.; Provost, N.; Nony, P.; Kleinschmidt, J. r.; Moullier, P.; Salvetti, A. Efficient recombinant adeno-associated virus production by a stable rep-cap HeLa cell line correlates with adenovirus-induced amplification of the integrated rep-cap genome. *J. Gene Med.* **2000**, *2*, 260−268.

(6) Nagy, A.; Chakrabarti, L.; Kurasawa, J.; Mulagapati, S. H. R.; Devine, P.; Therres, J.; Chen, Z.; Schmelzer, A. E. Engineered CHO cells as a novel AAV production platform for gene therapy delivery. *Sci. Rep.* **2023**, *13*, 19210.

(7) Smalley, E. First AAV gene therapy poised for landmark approval. *Nat. Biotechnol.* **2017**, *35*, 998−1000.

(8) Lemire, S.; Yehl, K. M.; Lu, T. K. Phage-based applications in synthetic biology. *Annu. Rev. Virol.* **2018**, *5*, 453−476.

(9) Lauring, A. S.; Jones, J. O.; Andino, R. Rationalizing the development of live attenuated virus vaccines. *Nat. Biotechnol.* **2010**, *28*, 573−579.

(10) Ungerechts, G.; Bossow, S.; Leuchs, B.; Holm, P. S.; Rommelaere, J.; Coffey, M.; Coffin, R.; Bell, J.; Nettelbeck, D. M. Moving oncolytic viruses into the clinic: clinical-grade production, purification, and characterization of diverse oncolytic viruses. *Mol. Ther. Methods. Clin. Dev.* **2016**, *3*, 16018.

(11) João, J.; Lampreia, J.; Prazeres, D. M. F.; Azevedo, A. M. Manufacturing of bacteriophages for therapeutic applications. *Biotechnol. Adv.* **2021**, *49*, No. 107758.

(12) Collins, L. T.; Ponnazhagan, S.; Curiel, D. T. Synthetic biology design as a paradigm shift toward manufacturing affordable adeno-associated virus gene therapies. *ACS Synth. Biol.* **2023**, *12*, 17−26.

(13) Oldfield, L. M.; Grzesik, P.; Voorhies, A. A.; Alperovich, N.; MacMath, D.; Najera, C. D.; Chandra, D. S.; Prasad, S.; Noskov, V. N.; Montague, M. G.; Friedman, R. M.; Desai, P. J.; Vashee, S. Genome-wide engineering of an infectious clone of herpes simplex virus type 1 using synthetic genomics assembly methods. *Proc. Natl. Acad. Sci. U. S. A.* **2017**, *114*, E8885−E8894.

(14) Charlton Hume, H. K.; Vidigal, J.; Carrondo, M. J.; Middelberg, A. P.; Roldão, A.; Lua, L. H. Synthetic biology for bioengineering virus-like particle vaccines. *Biotechnol. Bioeng.* **2019**, *116*, 919−935.

(15) Hamamoto, I.; Takaku, H.; Tashiro, M.; Yamamoto, N. High yield production of influenza virus in Madin Darby canine kidney (MDCK) cells with stable knockdown of IRF7. *PLoS One* **2013**, *8*, No. e59892.

(16) de Vries, W.; Haasnoot, J.; van der Velden, J.; van Montfort, T.; Zorgdrager, F.; Paxton, W.; Cornelissen, M.; van Kuppeveld, F.; de Haan, P.; Berkhout, B. Increased virus replication in mammalian cells by blocking intracellular innate defense responses. *Gene Ther.* **2008**, *7* (15), 545−552.

(17) Peng, R. W.; Guetg, C.; Tigges, M.; Fussenegger, M. The vesicle-trafficking protein munc18b increases the secretory capacity of mammalian cells. *Metab. Eng.* **2010**, *12*, 18−25.

(18) Liu, Y.; Zhang, Y.; Yao, L.; Hao, H.; Fu, X.; Yang, Z.; Du, E. Enhanced production of porcine circovirus type 2 (PCV2) virus-like particles in Sf9 cells by translational enhancers. *Biotechnol. Lett.* **2015**, *37*, 1765−1771.

(19) Gómez-Sebastián, S.; López-Vidal, J.; Escribano, J. M. Significant productivity improvement of the baculovirus expression vector system by engineering a novel expression cassette. *PLoS One* **2014**, *9*, No. e96562.

(20) Kirkwood, T. B.; Bangham, C. R. Cycles, chaos, and evolution in virus cultures: a model of defective interfering particles. *Proc. Natl. Acad. Sci. U. S. A.* **1994**, *91*, 8685−8689.

(21) Destro, F.; Barolo, M. A review on the modernization of pharmaceutical development and manufacturing-Trends, perspectives, and the role of mathematical modeling. *Int. J. Pharm.* **2022**, *620*, No. 121715.

(22) Bandiera, L.; Gomez-Cabeza, D.; Gilman, J.; Balsa-Canto, E.; Menolascina, F. Optimally designed model selection for synthetic biology. *ACS Synth. Biol.* **2020**, *9*, 3134−3144.
(23) Breitling, R.; Achcar, F.; Takano, E. Modeling challenges in the synthetic biology of secondary metabolism. *ACS Synth. Biol.* **2013**, *2*, 373−378.
(24) Duvigneau, S.; Dürr, R.; Laske, T.; Bachmann, M.; Dostert, M.; Kienle, A. Model-based approach for predicting the impact of genetic modifications on product yield in biopharmaceutical manufacturing—Application to influenza vaccine production. *PLOS Comput. Biol.* **2020**, *16*, No. e1007810.
(25) Handel, A.; Liao, L. E.; Beauchemin, C. A. Progress and trends in mathematical modelling of influenza A virus infections. *Curr. Opin. Syst. Biol.* **2018**, *12*, 30−36.
(26) Tapia, F.; Vázquez-Ramírez, D.; Genzel, Y.; Reichl, U. Bioreactors for high cell density and continuous multi-stage cultivations: options for process intensification in cell culture-based viral vaccine production. *Appl. Microbiol. Biotechnol.* **2016**, *100*, 2121−2132.
(27) Frensing, T.; Heldt, F. S.; Pflugmacher, A.; Behrendt, I.; Jordan, I.; Flockerzi, D.; Genzel, Y.; Reichl, U. Continuous influenza virus production in cell culture shows a periodic accumulation of defective interfering particles. *PLoS One* **2013**, *8*, No. e72288.
(28) Von Magnus, P. Incomplete forms of influenza virus. *Adv. Virus Res.* **1954**, *2*, 59−79.
(29) Rüdiger, D.; Pelz, L.; Hein, M. D.; Kupke, S. Y.; Reichl, U. Multiscale model of defective interfering particle replication for influenza A virus infection in animal cell culture. *PLOS Comput. Biol.* **2021**, *17*, No. e1009357.
(30) Haseltine, E. L.; Rawlings, J. B.; Yin, J. Dynamics of viral infections: incorporating both the intracellular and extracellular levels. *Comput. Chem. Eng.* **2005**, *29*, 675−686.
(31) Destro, F.; Joseph, J.; Srinivasan, P.; Kanter, J. M.; Neufeld, C.; Wolfrum, J. M.; Barone, P. W.; Springs, S. L.; Sinskey, A. J.; Cecchini, S.; Kotin, R. M.; Braatz, R. D. Mechanistic modeling explains the production dynamics of recombinant adeno-associated virus with the baculovirus expression vector system. *Molecular Therapy - Methods & Clinical Development* **2023**, *30*, 122−146.
(32) Grose, C.; Putman, Z.; Esposito, D. A review of alternative promoters for optimal recombinant protein expression in baculovirus-infected insect cells. *Protein Expression Purif.* **2021**, *186*, No. 105924.
(33) Treanor, J. J.; Schiff, G. M.; Hayden, F. G.; Brady, R. C.; Hay, C. M.; Meyer, A. L.; Holden-Wiltse, J.; Liang, H.; Gilbert, A.; Cox, M. Safety and immunogenicity of a baculovirus-expressed hemagglutinin influenza vaccine: a randomized controlled trial. *JAMA* **2007**, *297*, 1577−1582.
(34) López-Macías, C.; Ferat-Osorio, E.; Tenorio-Calvo, A.; Isibasi, A.; Talavera, J.; Arteaga-Ruiz, O.; Arriaga-Pizano, L.; Hickman, S. P.; Allende, M.; Lenhard, K.; Pincus, S.; Connolly, K.; Raghunandan, R.; Smith, G.; Glenn, G. Safety and immunogenicity of a virus-like particle pandemic influenza A (H1N1) 2009 vaccine in a blinded, randomized, placebo-controlled trial of adults in Mexico. *Vaccine* **2011**, *29*, 7826−7834.
(35) Smith, R. H.; Levy, J. R.; Kotin, R. M. A simplified baculovirus-AAV expression vector system coupled with one-step affinity purification yields high-titer rAAV stocks from insect cells. *Mol. Ther.* **2009**, *17*, 1888−1896.
(36) Rohrmann, G. F. *Baculovirus Molecular Biology*, 4th ed.; National Center for Biotechnology Information: Bethesda, MD, 2019.
(37) Rosinski, M.; Reid, S.; Nielsen, L. K. Kinetics of baculovirus replication and release using real-time quantitative polymerase chain reaction. *Biotechnol. Bioeng.* **2002**, *77*, 476−480.
(38) Morris, C. S.; Yoon, S. Modeling and optimization of continuous viral vaccine production. *Processes* **2022**, *10*, 2426.
(39) Vieira, H. L.; Estêvão, C.; Roldão, A.; Peixoto, C. C.; Sousa, M. F.; Cruz, P. E.; Carrondo, M. J.; Alves, P. M. Triple layered rotavirus VLP production: kinetics of vector replication, mRNA stability and recombinant protein production. *J. Biotechnol.* **2005**, *120*, 72−82.
(40) Cecchini, S.; Virag, T.; Kotin, R. M. Reproducible high yields of recombinant adeno-associated virus produced using invertebrate cells in 0.02- to 200-liter cultures. *Hum. Gene Ther.* **2011**, *22*, 1021−1030.
(41) Wu, C. P.; Chang, C. J.; Li, C. H.; Wu, Y. L. The influence of serial passage on the stability of an exogenous gene expression in recombinant baculovirus. *Entomol. Res.* **2021**, *51*, 168−175.
(42) De Gooijer, C. D.; Koken, R. H. M.; Van Lier, F. L. J.; Kool, M.; Vlak, J. M.; Tramper, J. A structured dynamic model for the baculovirus infection process in insect-cell reactor configurations. *Biotechnol. Bioeng.* **1992**, *40*, 537−548.
(43) Vignuzzi, M.; López, C. B. Defective viral genomes are key drivers of the virus-host interaction. *Nat. Microbiol.* **2019**, *4*, 1075−1087.
(44) Marriott, A. C.; Dimmock, N. J. Defective interfering viruses and their potential as antiviral agents. *Rev. Med. Virol.* **2010**, *20*, 51−62.
(45) Correia Ramos, J. R.; Bissinger, T.; Genzel, Y.; Reichl, U. Impact of influenza A virus infection on growth and metabolism of suspension MDCK cells using a dynamic model. *Metabolites* **2022**, *12*, 239.
(46) Kupke, S. Y.; Riedel, D.; Frensing, T.; Zmora, P.; Reichl, U. A novel type of influenza A virus-derived defective interfering particle with nucleotide substitutions in its genome. *J. Virol.* **2019**, *93*, 1786−1804.
(47) Zhao, H.; To, K. K.; Chu, H.; Ding, Q.; Zhao, X.; Li, C.; Shuai, H.; Yuan, S.; Zhou, J.; Kok, K. H.; Jiang, S.; Yuen, K. Y. Dual-functional peptide with defective interfering genes effectively protects mice against avian and seasonal influenza. *Nat. Commun.* **2018**, *9*, 2358.
(48) Dimmock, N. J.; Rainsford, E. W.; Scott, P. D.; Marriott, A. C. Influenza virus protecting RNA: an effective prophylactic and therapeutic antiviral. *J. Virol.* **2008**, *82*, 8570−8578.
(49) Rüdiger, D.; Kupke, S. Y.; Laske, T.; Zmora, P.; Reichl, U. Multiscale modeling of influenza a virus replication in cell cultures predicts infection dynamics for highly different infection conditions. *PLOS Comput. Biol.* **2019**, *15*, No. e1006819.
(50) Heldt, F. S.; Frensing, T.; Reichl, U. Modeling the intracellular dynamics of influenza virus replication to understand the control of viral RNA synthesis. *J. Virol.* **2012**, *86*, 7806−7817.
(51) Laske, T.; Heldt, F. S.; Hoffmann, H.; Frensing, T.; Reichl, U. Modeling the intracellular replication of influenza A virus in the presence of defective interfering RNAs. *Virus Res.* **2016**, *213*, 90−99.
(52) Laske, T.; Bachmann, M.; Dostert, M.; Karlas, A.; Wirth, D.; Frensing, T.; Meyer, T. F.; Hauser, H.; Reichl, U. Model-based analysis of influenza A virus replication in genetically engineered cell lines elucidates the impact of host cell factors on key kinetic parameters of virus growth. *PLOS Comput. Biol.* **2019**, *15*, No. e1006944.
(53) Hein, M. D.; Arora, P.; Marichal-Gallardo, P.; Winkler, M.; Genzel, Y.; Pöhlmann, S.; Schughart, K.; Kupke, S. Y.; Reichl, U. Cell culture-based production and in vivo characterization of purely clonal defective interfering influenza virus particles. *BMC Biol.* **2021**, *19*, 91.
(54) Wagner, E. K.; Petroski, M. D.; Pande, N. T.; Lieu, P. T.; Rice, M. Analysis of factors influencing kinetics of herpes simplex virus transcription utilizing recombinant virus. *Methods* **1998**, *16*, 105−116.
(55) Zhang, H.; Xie, J.; Xie, Q.; Wilson, J. M.; Gao, G. Adenovirus-adeno-associated virus hybrid for large-scale recombinant adeno-associated virus production. *Hum. Gene Ther.* **2009**, *20*, 922−929.
(56) Hein, M. D.; Chawla, A.; Cattaneo, M.; Kupke, S. Y.; Genzel, Y.; Reichl, U. Cell culture-based production of defective interfering influenza A virus particles in perfusion mode using an alternating tangential flow filtration system. *Appl. Microbiol. Biotechnol.* **2021**, *105*, 7251−7264.
(57) Joshi, P. R.; Venereo-Sanchez, A.; Chahal, P. S.; Kamen, A. A. Advancements in molecular design and bioprocessing of recombinant adeno-associated virus gene delivery vectors using the insect-cell baculovirus expression platform. *Biotechnol. J.* **2021**, *16*, No. 2000021.
(58) Joshi, P. R.; Cervera, L.; Ahmed, I.; Kondratov, O.; Zolotukhin, S.; Schrag, J.; Chahal, P. S.; Kamen, A. A. Achieving high-yield

production of functional AAV5 gene delivery vectors via fedbatch in an insect cell-one baculovirus system. *Mol. Ther. Methods Clin. Dev.* **2019**, *13*, 279−289.
(59) Huang, I.-C.; Li, W.; Sui, J.; Marasco, W.; Choe, H.; Farzan, M. Influenza A virus neuraminidase limits viral superinfection. *J. Virol.* **2008**, *82*, 4834−4843.
(60) Lama, J. The physiological relevance of CD4 receptor down-modulation during HIV infection. *Curr. HIV Res.* **2005**, *1*, 167−184.



https://doi.org/10.1021/acssynbio.4c00227
*ACS Synth. Biol.* 2024, 13, 3173−3187